Optic nerve sheath fenestration using a Raman-shifted alexandrite laser

John Kozub, PhD[1], **Jin-H. Shen, PhD**[2,3], **Karen M. Joos, MD, PhD**[2,3,4], **Ratna Prasad, PhD**[2], and **M. Shane Hutson, PhD**[1,4,5,*]

[1]Department of Physics & Astronomy (JK,MSH), Vanderbilt University, Nashville, TN 37235, USA

[2]Vanderbilt Eye Institute (JHS,KMJ,RP), Vanderbilt University, Nashville, TN 37235, USA

[3]Vanderbilt Institute in Surgery and Engineering (JHS,KMJ), Vanderbilt University, Nashville, TN 37235, USA

[4]Vanderbilt Biophotonics Center (KMJ,MSH), Vanderbilt University, Nashville, TN 37235, USA

[5]Vanderbilt Institute for Integrative Biosystem Research & Education (MSH), Vanderbilt University, Nashville, TN 37235, USA

Abstract

Background and Objective—Optic nerve sheath fenestration is an established procedure for relief of potentially damaging overpressure on the optic nerve resulting from idiopathic intracranial hypertension. Prior work showed that a mid-IR free-electron laser could be delivered endoscopically and used to produce an effective fenestration. This study evaluates the efficacy of fenestration using a table-top mid-IR source based on a Raman-shifted alexandrite (RSA) laser.

Study Design/Materials and Methods—Porcine optic nerves were ablated using light from an RSA laser at wavelengths of 6.09, 6.27 and 6.43 μm and pulse energies up to 3 mJ using both free-space and endoscopic beam delivery through 250-μm I.D. hollow-glass waveguides. Waveguide transmission was characterized, ablation thresholds and etch rates were measured, and the efficacy of endoscopic fenestration was evaluated for *ex vivo* exposures using both optical coherence tomography and histological analysis.

Results—Using endoscopic delivery, the RSA laser can effectively fenestrate porcine optic nerves. Performance was optimized at a wavelength of 6.09 μm and delivered pulse energies of 0.5-0.8 mJ (requiring 1.5-2.5 mJ to be incident on the waveguide). Under these conditions, the ablation threshold fluence was 0.8 ± 0.2 J/cm^2, the ablation rate was 1-4 μm/pulse, and the margins of ablation craters showed little evidence of thermal or mechanical damage. Nonetheless, nominally identical exposures yielded highly variable ablation rates. This led to fenestrations that ranged from too deep to too shallow – either damaging the underlying optic nerve or requiring additional exposure to cut fully through the sheath. Of 48 excised nerves subjected to fenestration at 6.09 μm, 16 *ex vivo* fenestrations were judged as good, 23 as too deep, and 9 as too shallow.

---

*Corresponding Author: M. Shane Hutson, VU Station B 351807, Nashville, TN 37235, Phone: 615-343-9980; Fax: 615-343-7263, shane.hutson@vanderbilt.edu.

Conclusions—Mid-IR pulses from the RSA laser, propagated through a flexible hollow waveguide, are capable of cutting through porcine optic nerve sheaths in surgically relevant times with reasonable accuracy and low collateral damage. This can be accomplished at wavelengths of 6.09 or 6.27 μm, with 6.09 μm slightly preferred. The depth of *ex vivo* fenestrations was difficult to control, but excised nerves lack a sufficient layer of cerebrospinal fluid that would provide an additional margin of safety in actual patients.

Keywords

ablation; laser surgery; mid-infrared; free-electron laser; pseudotumor cerebri; idiopathic intracranial hypertension

INTRODUCTION

Pseudotumor cerebri or idiopathic intracranial hypertension (IIH) is a condition involving increased fluid pressure around the brain and optic nerve (1). The increased pressure can damage the optic nerve and lead to permanent and severe vision loss (2,3). One treatment option for IIH is optic nerve sheath fenestration – literally cutting a small window or slits in the optic nerve's surrounding connective tissue (4). Conventional fenestration accesses the optic nerve by disinserting and later reinserting the orbit's medial rectus muscle, a procedure with extended recovery times (4). To develop a less invasive laser-based technique, previous investigators explored the potential of a mid-infrared (mid-IR) free-electron laser (FEL). When the FEL was tuned to appropriate wavelengths in the 6- to 7-μm range – targeting the strong and overlapping vibrational absorption bands corresponding to the H-O-H bending mode of water and the amide I and II modes of tissue proteins (5) – it was able to cut precise incisions in optic nerve sheaths without damaging the underlying optic nerve (6). Such laser fenestrations were performed successfully in rabbits (6), monkeys (7), and in a limited trial in human patients (8,9). Previous work also showed that fenestration could be accomplished less invasively and without disinserting extraocular muscles if done through an orbital endoscope using pulses from a mid-IR FEL (10). Unfortunately, mid-IR FELs require large dedicated operational facilities and are expensive to both build and maintain – preventing these laser systems from finding widespread use in patient care.

Following these initial demonstrations, multiple groups evaluated the potential of several alternative mid-IR lasers (11-15). To date, three systems have ablated soft tissues cleanly and efficiently enough to warrant follow-up investigations: an Er:YAG-pumped optical parametric oscillator (12); a Nd:YLF-based system that converts near-IR light to mid-IR wavelengths using stimulated Raman scattering and difference frequency mixing (13); and an alexandrite-based system that uses two stages of Raman conversion to reach wavelengths in the 6- to 7-μm range (14,16). Only the last of these three has achieved sufficient energy per pulse and sufficient average power to cut soft tissues at rates that make surgical applications feasible (14). This capability has recently been quantified with regards to cornea and gelatin (17). These are model tissues/phantoms that bracket the range of mechanical properties found among soft tissues, but that are not directly relevant to specific surgical applications for mid-IR lasers. Here, we evaluate the performance of a Raman-shifted alexandrite (RSA) laser for endoscopic fenestrations of excised porcine optic nerve

sheaths. We find that mid-IR pulses from the RSA laser, propagated through a flexible hollow-glass waveguide, are capable of cutting through porcine optic nerve sheaths in surgically relevant times with reasonable accuracy and very little collateral damage. We quantify the ablation metrics needed to plan such procedures and note that fenestrations can be accomplished at wavelengths of 6.09 or 6.27 μm, with 6.09 μm slightly preferred. For the *ex vivo* procedures evaluated here, nominally identical exposures yield fenestrations that range from too shallow to too deep – the latter damaging the underlying optic nerve. This problematic variability arises specifically for *ex vivo* procedures due to a combination of sample-to-sample variations in sheath thickness, pulse-to-pulse fluctuations of laser energy, and the lack of a sufficient intervening layer of cerebrospinal fluid. For patients with IIH, this layer would be much thicker and provide a much larger margin of safety.

MATERIALS AND METHODS

Raman-shifted alexandrite laser

These experiments were conducted using a Raman-shifted alexandrite (RSA) laser developed by Light Age Inc. (Somerset, NJ) as a prototype of its Advanced Mid-IR (AMIR™) laser system. In brief, this system is based on a Q-switched alexandrite laser (101-PAL™, Light Age Inc.) whose near-IR output (771-785 nm) is serially converted to mid-IR wavelengths in the 6- to 7-μm range using Raman scattering in a two-pass deuterium cell and a multi-pass hydrogen cell. Additional laser details and operational characteristics have been published previously (14). The laser's mid-IR output had a pulse repetition rate of 10 Hz, pulsewidths of ~25 ns as measured using a photoelectromagnetic detector (PEM-1, Boston Electronics, Brookline, MA), and a spectral bandwidth of 10-15 nm FWHM as measured using a monochromator with a linear pyroelectric array (Spiricon LP-256-12-BaF_2, Ophir-Spiricon LLC, Logan, UT). Proper alignment of the multi-pass converter was verified prior to each experiment by optimizing the spatial beam profile of the mid-IR output with a pyroelectric array camera (Pyrocam III, Ophir Optronics, North Logan, UT). The maximum pulse energies available from the RSA laser used for this work varied from ~3.0 mJ for wavelengths around 6.1 μm to only ~1.0 mJ for those near 6.45 μm. When optimally tuned for a specific wavelength, the standard deviation of the mid-IR pulse energy was ~25-45% (17). This variability could be traced back to fluctuations in the flashlamp pump energy of the alexandrite laser that then propagated through the nonlinear Raman conversion processes.

Optic nerve sheath sample preparation

Porcine cadaver eyes were obtained less than 24 hours postmortem from animals euthanized for other IACUC-approved protocols by the Vanderbilt Division of Animal Care. Muscle and fatty tissue were removed and the exposed nerve excised from the eyeball; prepared nerves were surrounded with excised fat and muscle tissue, and were kept cold until just before use. A section of silicone tubing (¼" I.D. × ½" O.D.), sliced in half lengthwise, was used to hold the excised nerve in place for exposure to laser pulses. For free-space laser delivery, the top surface of each nerve was positioned (using a micrometer-driven stage) at the exact height above the table corresponding to the waist of the focused laser beam. For

delivery through hollow glass waveguides, the top surface of the nerve was positioned 3-4 mm from the end of the waveguide.

Laser exposure conditions for free-space delivery

The RSA laser was operated at a repetition rate of 10 Hz and focused to a 300- $\pm$ 20-μm diameter spot using a 200-mm focal length CaF_2 lens. The beam was turned downward toward the sample surface with a silver mirror. A beamsplitter was used to reflect a small percentage of the mid-IR light toward a sensitive energy probe (Molectron J10, Coherent Inc., Santa Clara, CA) connected to a joulemeter (Molectron EPM2000, Coherent Inc., Santa Clara, CA) to measure laser pulse energies during exposures. A HeNe laser beam, reflected from the beamsplitter, was co-aligned with the mid-IR pulses to visually identify the targeted spot. The exact location and size of the beam waist were determined using a knife-edge scanning technique to map out the beam diameter as a function of height above the table. The surface of the optic nerve was positioned at the location of the minimum spot diameter. This positioning was done immediately before exposure to RSA laser pulses.

Laser exposure conditions for endoscopic waveguide delivery

RSA laser pulses were coupled into 250-μm I.D. hollow-glass waveguides coated for high reflectivity in the mid-IR (fabricated by James A. Harrington, Rutgers University). Optimal coupling of mid-IR output from the RSA laser into the waveguides required correction of the beam's observable astigmatism. This was accomplished using a telescope installed before the multi-pass converter. Light was then coupled into waveguides using a single BaF_2 or CaF_2 focusing lens. The input end of each waveguide was aligned to the waist of the focused mid-IR beam using an optical fiber positioner with 3-axis translation and angular capability. To assist in alignment of the waveguide opening, a HeNe laser was reflected from a BaF_2 beamsplitter to co-align with the mid-IR beam. After preliminary testing, we selected the three 1.5-m long waveguides that best transmitted RSA laser pulses at 6.09 μm and used these for all subsequent tasks.

Waveguide transmission was measured using a ratiometer setup with a beamsplitter, two energy probes (Molectron J10, Coherent Inc., Santa Clara, CA), and a two-channel, computer-interface joulemeter (Molectron EPM2000, Coherent Inc., Santa Clara, CA). For each measurement, the transmission ratio was averaged over 500 pulses. Reproducible 90° bends in one waveguide were made by holding it against the curved edge of various cylindrical objects having different radii of curvature.

Laser pulses incident on a waveguide were monitored and controlled as described for free-space delivery. The output end of the waveguide was directed downward using a gentle bend and the surface of the optic nerve was positioned 3-4 mm from the end of the waveguide. The best output energy attained through a 1.5-m length of waveguide was ~30% of the input energy. Output pulse energies from the waveguide had a slightly higher variance than the input energies, due to coupling losses from fluctuations in the input beam profile and to a slight pointing instability of the RSA output. The beam diameter, measured 3.5 mm from the end of the waveguide, was determined to be 200 $\pm$ 20 μm by a knife-edge scanning technique.

Measurement of ablation thresholds

Ablation threshold is defined here as the energy for which a single laser pulse has a 50% probability of ejecting material that is detectable using brightfield illumination. Ablation thresholds were determined using probit analysis (18) and conducted in Mathematica (Wolfram Inc., Champagne, IL) as described previously (17).

Measurement of ablation rates

A predetermined number of laser pulses (at 10 pulses per second) were delivered to a single spot on the surface of excised optic nerve sheaths with exposure controlled using a fast shutter and a custom LabView program (National Instruments, Austin, TX). This program also interfaced with the energy probe and joulemeter to record the actual pulse energies delivered during each exposure (a few exceptions in which we did not record the actual pulse energies are noted in Results below). Each nerve was translated along its length by 1.0-mm increments between laser exposures. To limit dehydration of exposed nerve sheaths, only 6-8 ablation craters were made in each nerve over the course of just 2-3 minutes. Ablated nerves were immediately imaged using an OCT (optical coherence tomography) system (Bioptigen, Morrisville, NC), and the resulting images were later used to determine the depth of each crater. Plots of crater depth versus number of laser pulses appeared reasonably linear until the laser fully perforated a nerve sheath. We thus estimated etch rates via linear regression of the data collected prior to sheath perforation.

Histological assessment of collateral damage

Selected optic nerves were subjected to single-point ablations and then immediately preserved in Pen-Fix. The fixed nerves were later stained with hematoxylin and eosin (H&E) and imaged on an Olympus AX70 microscope (Olympus, Center Valley, PA) for histological analysis to evaluate thermal and mechanical damage. Image analysis was conducted in ImageJ (NIH, Bethesda, MD).

Endoscopic fenestration of porcine optic nerve sheaths

Porcine optic nerves were obtained and prepared as described above. Circular fenestrations were then performed using the RSA laser output tuned to a wavelength of either 6.09 or 6.27 μm and delivered to the sample through a 1.5-m long, 250-μm I.D. hollow-glass waveguide housed within an endoscope. The fenestrations were cut free hand in three circular passes taking approximately 1.5 minutes. Fenestrated nerves were examined immediately by OCT with selected nerves then fixed and H&E stained for histological analysis.

RESULTS

The results reported here are designed to provide all the measurements needed to plan and evaluate endoscopic optic nerve sheath fenestrations using an RSA laser. We thus characterize transport of RSA laser pulses through the hollow glass waveguides used for endoscopic beam delivery and determine optimal laser parameters for ablating optic nerve sheath (wavelength, spot size, and mean pulse energy). Using these laser parameters, we then evaluate collateral damage and the accuracy of fenestration in excised optic nerve specimens.

Note that water vapor absorption severely restricts the pulse energies attainable with the RSA laser at many wavelengths in the 6- to 7-μm range (17). This limitation makes it necessary to slightly detune the laser from the exact peaks of the targeted tissue absorption bands. For example, we could not attain sufficient pulse energy to reliably ablate tissue at the peak of the amide I absorption band at 6.10 μm, but we could at 6.09 μm. The targeted tissue absorption bands are spectrally broad (~200 nm FWHM) and we thus expect no differences in the laser-tissue interactions for the detuned wavelengths investigated here (6.09, 6.27 and 6.43 μm).

Optimization of waveguide coupling efficiency and transmission

The maximum transmission of RSA laser pulses through 1.5-m lengths of a 250-μm I.D. hollow-glass waveguide was about 30% of the energy incident on the coupling lens. This efficiency was consistently achieved with the waveguide input end positioned near the beam waist after focusing with a single 150-mm focal length CaF_2 lens. Coupling with stronger (100-mm) or weaker (200-mm) lenses was less efficient. A clean, square cut in the waveguide end was required for good coupling efficiency, and since the laser spot diameter was roughly equal to the waveguide's inner diameter, coupling was extremely sensitive to alignment of the waveguide opening. Misalignment was clearly indicated by a snapping sound produced when high intensity light encountered the edge of the waveguide. Even after proper alignment, pulse-to-pulse changes in laser beam profile (clearly observed with a pyroelectric array camera) and occasional changes in pointing stability could misalign the waveguide, leading to significant fluctuations in waveguide transmission, and gradually degrading the waveguide end. Maximum transmission could be restored by removing 2-3 mm of the damaged end and realigning the laser through the coupling lens.

To estimate waveguide coupling efficiency, we sacrificed one known good waveguide to measure the transmission of RSA laser pulses through successively shorter straight sections. These measurements were conducted using two wavelengths (6.09 and 6.27 μm) and two different nominal incident pulse energies (~2.7 and ~1.5 mJ/pulse). Waveguide transmission was fit to an exponential decay as a function of waveguide length (Figure 1). These fits yielded transmission decay lengths of 200-250 cm and coupling efficiencies near 0.5. The measured parameters are presented in Table 1.

For endoscopic delivery of laser energy to the optic nerve in patients, the waveguide will have to bend around the eyeball. We thus measured the laser energy transmitted through a 1.5-m length of a waveguide with one 90° bend. Gentle bends (radius of curvature R 30 cm) had no significant effect on transmission. Sharper bends did degrade transmission efficiency, but even the smallest bend radius considered safe for the waveguide ($R = 4.6$ cm) only decreased transmission from 30% to 21-23% (Figure 1, data points marked with U symbols).

Through each of these characterizations, the 250-μm I.D. hollow-glass waveguides were robust and provided fairly efficient transmission of mid-IR laser pulses – nearly identical to that found previously for FEL pulses at similar wavelengths (19). Bending losses were acceptable for making a hand-held probe for delivery around an eyeball within its orbit and the largest limitation was the limited coupling efficiency of just ~0.5. For the two

wavelengths and limited pulse energies tested, there was a marginal difference in coupling efficiency (slightly better for 6.09 μm), but there were no significant differences in transmission decay length or bending losses.

Ablation thresholds

As a first step toward selecting optimal laser parameters for fenestration, we measured ablation thresholds for optic nerve sheaths using our targeted wavelengths. When delivering laser energy through a 1.5-m long, 250-μm I.D. hollow glass waveguide, we found a significant wavelength dependence; the lowest ablation threshold was for 6.09 μm, and the ablation threshold at 6.27 μm was roughly twice as high. For this length of waveguide, the transmitted laser energy was not sufficient to accurately measure the threshold at 6.43 μm. We were however able to just measure the 6.43-μm threshold using beam delivery through a very short length of waveguide (8 cm). To convert these threshold energies to fluences, we measured the spot diameter 3.5 mm from the end of the waveguide and found it to be 200 ± 20 μm. To facilitate comparison with previous measurements on other soft tissues, we also measured thresholds using free space delivery to a focused spot diameter of 300 ± 20 μm. Under these conditions, we observed a similar doubling of the threshold for 6.27 versus 6.09 μm, but sufficient laser energy was not available to accurately measure the threshold at 6.43 μm. Table 2 summarizes the measured ablation thresholds. For each of the tested wavelengths and both spot sizes, the threshold fluences are slightly higher than those found previously for RSA laser ablation of cornea (17).

Under both exposure conditions, a clear wavelength-dependence was found for the ablation threshold of optic nerve sheath. Although these wavelengths target tissue protein and water absorption bands to different degrees, the trends in ablation threshold largely follow the overall tissue absorption coefficients – lower thresholds for more strongly absorbed wavelengths. Interestingly, the threshold also depends strongly on delivery method and/or spot size. The threshold energy is two times higher for waveguide delivery to a smaller 200-μm diameter spot. The combination means that the more tightly focused exposure requires a threshold fluence that is 4-5x higher. This result is consistent with previous ablation measurements using a mid-IR FEL that showed a strong increase in threshold fluence for smaller spot sizes (20). An additional contribution to the increased thresholds may arise from changes in the beam's spatial intensity distribution. The values noted in Table 2 are in terms of average fluence, but peak fluence may be more critical – especially at threshold. Transmission through the waveguide flattens the beam profile and brings the peak fluence closer to the average fluence. In an ideal case comparing Gaussian and top-hat profiles, this difference in peak versus average fluence could contribute a factor of two difference in reported thresholds.

Ablation rates

The rates at which RSA laser pulses ablated porcine nerve sheaths were estimated using OCT images collected immediately after ablation on unfixed tissue. Since we were directly interested in the ablation rate for optic nerve sheath, we excluded craters that cut through a sheath and into the underlying nerve. This was an unfortunately frequent occurrence because porcine optic nerve sheaths are quite thin – 100- to 150-μm thick on average – with variable

thickness along the length of each nerve. They are also easily damaged during pre-ablation removal of surrounding fatty tissue. We found it impractical to evaluate sheath thickness and condition before laser exposure because the few minutes needed to collect OCT images also allowed *ex vivo* nerves to dry out. The combination of a thin or dry sheath and too many laser pulses resulted in complete perforation of the sheath and penetration into the underlying nerve. We did not rehydrate sheaths because doing so with normal saline resulted in swelling of the sheath beyond its original thickness. Our experimental protocol was thus to prepare an optic nerve sample, quickly ablate a series of craters at different positions along its length, and immediately take OCT images of each crater. These post-ablation OCT images were then used to evaluate sheath condition and the extent of ablation. Craters were excluded from further analysis when a nerve sheath could not be clearly distinguished in OCT images, when a nerve sheath had obviously dried out during an experiment, or when ablation proceeded into the underlying nerve. This last exclusion criterion was the most difficult to evaluate because laser-damaged nerve tissue tended to swell and partially or completely fill the ablation crater – making it difficult, but not impossible to distinguish cuts that fully perforated the sheath.

With these caveats, we report here the range of ablation rates typically observed for a given average pulse energy. Previous investigations in cornea samples noted a high degree of variability in the etch rates, especially when the beam was tightly focused (~ 100-μm spot diameter; 17). We thus avoided such tight focusing here, but even when a good sheath was ablated with a larger spot size and an appropriate total dose of laser energy, the depth of the resulting cut and the apparent etch rate were highly variable – both over a single nerve, and from one nerve to the next. For free-space beam delivery, wavelengths of 6.09 or 6.27 μm, and average pulse energies well above threshold (0.7-1.3 mJ), we found variable ablation rates from 1-6 μm/pulse. If we increased the pulse energy to 1.5-1.8 mJ, the laser completely perforated the nerve sheath within 1-2 seconds – just 10-20 pulses – and clearly damaged the underlying nerve tissue. If we dropped the pulse energy to near threshold, tissue removal became erratic, unreliable, and slow. Similar results were obtained for waveguide delivery of the beam, with perforation occurring frequently for pulse energies in the range of 0.85-1.0 mJ. Compared to free-space delivery conditions, this is at a lower pulse energy, but higher pulse fluence. Typical ablation rates for each set of conditions are summarized in Table 3. Note that we were unable to deliver enough energy at 6.43 μm to yield any measureable tissue removal.

With either 6.09- or 6.27-μm laser pulses and with either delivery method, there was a range of pulse energies between threshold and the occurrence of rapid perforation over which individual nerve sheaths yielded a roughly linear relationship between the number of pulses delivered (N_p) and the resulting crater depth ( ). Examples for both free-space and waveguide delivery are shown in Figure 2A and E. Both examples show some evidence that (N_p) becomes slightly sub-linear for the highest numbers of pulses. Nonetheless, the fitted etch rate (δ) was determined by the slope of the best-fit regression line (with fixed zero offset).

The dependence of ablation rate on average pulse energy ($<\varepsilon>$) is summarized in Figure 2 with panels C and G plotting the fitted etch rate for multiple craters ablated in single sheaths

at the same nominal pulse energy (11 sheaths for free-space delivery and 17 for waveguide delivery) and with panels D and H plotting the individual etch rates (δ/N_p) for every measured crater (144 craters for free-space delivery and 423 for waveguide delivery). As expected, the etch rates increase with average pulse energy, but with a high degree of variability.

Visual inspection of the free-space ablation rates in Figure 2C and G appear to show a slight wavelength dependence. To evaluate this dependence, we fit $\delta(<\varepsilon>)$ to two different models: a two-parameter, λ-independent model in which the etch rate was a linear function of average pulse energy, $\delta = \alpha(<\varepsilon>) - \varepsilon_0)$; and a four-parameter model in which both α and ε_0 were λ-dependent. In both cases, each parameter was constrained to be positive. We then used the Akaike Information Criterion, corrected for finite sample size (AICc), to evaluate information loss and relative model quality. AICc is a well-established measure of the information lost when goodness-of-fit is improved by using a model with more parameters (21). For both free-space and waveguide delivery, we found a much lower AICc (less information loss) and thus a preference for the λ-independent models ($\Delta_{AICc,free} = 32.1$; $\Delta_{AICc,wg} = 13.8$). This statistical measure does not imply a complete lack of wavelength dependence, only that one cannot be firmly established given the large sample-to-sample variability and limited number of samples. The best-fit λ-independent models are

$$\delta_{\text{free- space}} = \left(2.6 \pm 1.0 \tfrac{\mu m/\text{pulse}}{mJ}\right)\left(\langle\varepsilon\rangle - (0.0 \pm 0.5 \quad mJ)\right)$$
$$\delta_{\text{waveguide}} = \left(6.5 \pm 1.2 \tfrac{\mu m/\text{pulse}}{mJ}\right)\left(\langle\varepsilon\rangle - (0.4 \pm 0.1 \quad mJ)\right)$$

These are overlaid on the data to which they were fit in Figure 2C and G and repeated for the alternative compilation of fitted etch rates in Figure 2D and H. Note that the shaded areas in Figure 2 denote the 95% single prediction confidence bands and show that there is considerable uncertainty in the expected etch rate for a given nominal pulse energy. Nonetheless, using free-space delivery and a 300-μm spot diameter, the etch rates for optic nerve sheath are similar to those measured previously for both gelatin and cornea (17). Interestingly, the best-fit values for α show that ablation with the more tightly focused waveguide-delivered beam is more than twice as strongly dependent on pulse energy. This interplay of spot-size and pulse energy in determining etch rates qualitatively matches previous observations, but the trend observe here for optic nerve sheath is stronger than that seen for gelatin samples and weaker than that observed for cornea (17).

Assessment of collateral damage from single-point ablation

In order to evaluate potential collateral damage for a worst-case scenario, we ablated optic nerve sheaths with exposure directed at a single point. These single-point craters were then fixed and H&E stained for histology, allowing evaluation of collateral damage to the sheath and underlying nerve from both pressure waves and accumulated heat. In this exposure protocol, laser pulses are directed to the same spot at a repetition rate of 10 Hz for several seconds. In contrast to a fenestration in which the laser is scanned along a larger circular arc, these repeated exposures at the same location allow the accumulation of residual thermal

energy from multiple laser pulses and should thus err towards overestimating the thermal damage expected during an actual fenestration procedure.

We exposed several nerve sheaths to waveguide-delivered pulses (spot diameter 200 μm) at wavelengths of 6.09 or 6.27 μm. For both wavelengths, thermal collateral damage of the nerve sheath itself was minimal. We observed no increase in H&E staining (typically interpreted as excess binding of the dye to denatured proteins), and only a slight thickening or swelling of the nerve sheath near the edge of the crater. The degree of collateral damage was similar to that observed previously for RSA laser ablation of cornea (17). As for the underlying optic nerve, we observed no thermal damage or visible structural damage so long as laser exposure was at low energy and did not continue after the sheath was perforated (Figure 3A). If laser exposure continued after sheath perforation, the underlying nerve tissue suffered one or more of several types of damage: compression (Figure 3B); disruption of the tissue (Figure 3C); or swelling with a reduction in histologically observed tissue density (Figure 3D). If higher pulse energy was used, both compression damage (Figure 3E), and penetration into the nerve (Figure 3F) were more likely.

Assessment of optimal laser parameters

The clearest conclusion from the ablation metrics measured above is that the pulse energies currently attainable near 6.45 μm are insufficient for reliable ablation. On the other hand, the differences between wavelengths of 6.09 and 6.27 μm were subtle. Certainly, the ablation threshold was less for 6.09 μm at both tested spot sizes; however, for pulse energies well above threshold, the ablation rates had no discernable wavelength dependence, especially using waveguide beam delivery. Furthermore, histology of single-point ablation craters using both wavelengths indicated very low collateral damage to optic nerves as long as the sheath was not perforated during exposure. Both wavelengths are thus good candidates for use in optic nerve sheath fenestration.

Ex vivo endoscopic optic nerve sheath fenestration

Since even histology of single point perforations of the optic nerve showed very little difference when using wavelengths of 6.09 or 6.27 μm, we chose to evaluate both wavelengths for their ability to perform *ex vivo* optic nerve sheath fenestrations. Figure 4 shows an example brightfield image of an exposed optic nerve immediately after fenestration (the overlain arrows point to the circular incision). Overall, we find optimal fenestration of porcine cadaver optic nerve sheaths for λ = 6.09 μm and pulse energies of 0.5-0.8 mJ. Even under these conditions, we observed energy fluctuations that led to a mix of fenestration quality – some were ideal, some too shallow, and some too deep.

The quality of each attempted fenestration was evaluated using OCT images taken within a few minutes of ablation. Examples are shown in Figure 5. Fenestrations were judged as "good" if a circular cut was made through the sheath without damaging the underlying nerve, "deep" if the underlying optic nerve was damaged, and "superficial" if the sheath was not completely incised. If the cut was superficial only in some areas, the remaining cap of nerve sheath could potentially be removed with forceps. The distribution of fenestration quality for 59 mock *ex vivo* surgeries is compiled in Table 4.

Approximately 1/3 of all attempted fenestrations were successful at both wavelengths. There was a tendency for ablation to err on the side of going too deep at 6.09 μm and to remain too shallow at 6.27 μm – largely a consequence of the pulse energies used. Through careful analysis of the pulse energies used in each experiment, we find that the optimal conditions for endoscopic fenestration of porcine cadaver nerve sheaths using a 250-μm I.D. waveguide are a wavelength of 6.09 μm and pulse energies between 0.5 to 0.8 mJ. Lower pulse energies are too close to the ablation threshold and do not cut reliably; higher energies cut too quickly, risking rapid perforation of the sheath and damage to the underlying nerve. Example histological images for ideal, deep and superficial fenestrations are shown in Figure 6. For appropriately controlled fenestrations, there is no evidence of damage to the underlying nerve. As shown in Figure 2B and F, each excised optic nerve and its overlying sheath are separated by negligible cerebrospinal fluid; the extent of the fluid layer between nerve and sheath would be indicated by a hypo-reflective space in OCT images. Its negligible thickness here, due to fluid leakage from both ends of the excised nerves, makes *ex vivo* fenestrations an exceptionally challenging test of the laser's surgical capabilities.

DISCUSSION

Our overall conclusion is that mid-IR laser pulses from the RSA laser, propagated through a flexible hollow waveguide, are capable of cutting through porcine optic nerve sheaths in surgically relevant times with very low thermal collateral damage. This can be accomplished at wavelengths of 6.09 or 6.27 μm. Our results suggest that the laser parameters best suited to this task are a wavelength of 6.09 μm and pulses of 0.5-0.8 mJ delivered through a 250-μm I.D. hollow-glass waveguide. This combination yields ablation rates of 3-5 μm/pulse (30-50 μm/s at 10 Hz) and can complete a circular fenestration in 1-2 minutes.

The *ex vivo* fenestrations evaluated here are an exceptionally difficult challenge; their success rate was low because the sheath thickness varied within and between samples, because the laser energy and ablation rate fluctuated from pulse to pulse, and because the excised samples had negligible layers of cerebrospinal fluid that provided little margin for error. For those *ex vivo* fenestrations that did stop before ablating the underlying nerve, we observed a minimal degree of thermal and mechanical collateral damage. The RSA laser thus still holds promise for endoscopic fenestrations in IIH patients because there are paths that may overcome each of the remaining limitations.

First, the thin layer of cerebrospinal fluid is specific to excised porcine optic nerves. This layer would be thicker in human patients – particularly those suffering from IIH where it is often > 2 mm thick (22). A thicker cerebrospinal fluid layer would provide a larger margin of safety for laser pulses to ablate through the sheath and into the fluid layer, but not into the underlying nerve.

A larger margin of safety would certainly help, but even under nominally identical exposure conditions, large variability remains in the etch rate from one nerve to the next and even for different craters along the length of a single nerve. All of this variability can be summarized in the confidence intervals of the overall linear regressions shown in Figure 2. Future reductions in pulse-to-pulse energy fluctuations could improve fenestration outcomes;

however, ablation with mid-IR lasers is based on explosive vaporization and the inherent stochasticity of this mechanism will continue limiting the predictability of crater depths. A fully realized endoscopic fenestration system will thus likely need to incorporate look-ahead imaging to monitor progress toward perforating a nerve sheath. Several methods could provide such imaging capabilities – e.g., endoscopic OCT (23,24) or inline coherent imaging (25). Combined with improvements in laser pulse consistency and larger *in vivo* margins for safety, the RSA laser could provide a means to perform optic nerve sheath fenestrations using an endoscopic approach in IIH patients.

ACKNOWLEDGEMENTS

REFERENCES

1. Binder DK, Horton JC, Lawton MT, McDermott MW. Idiopathic intracranial hypertension. Neurosurgery. 2004; 54(3):538–551. discussion 551-532. [PubMed: 15028127]

2. Ahlskog JE, O'Neill BP. Pseudotumor cerebri. Ann Intern Med. 1982; 97(2):249–256. [PubMed: 7049034]

3. Maus M, Sergott RC. Optic nerve sheath decompression: a review. Int Ophthalmol Clin. 1992; 32(3):179–196.

4. Corbett JJ, Nerad JA, Tse DT, Anderson RL. Results of optic nerve sheath fenestration for pseudotumor cerebri. The lateral orbitotomy approach. Arch Ophthalmol. 1988; 106(10):1391–1397. [PubMed: 3273487]

5. Edwards G, Logan R, Copeland M, Reinisch L, Davidson J, Johnson B, Maciunas R, Mendenhall M, Ossoff R, Tribble J, Werkhaven J, O'Day D. Tissue Ablation by a Free-Electron Laser Tuned to the Amide-II Band. Nature. 1994; 371(6496):416–419. [PubMed: 8090220]

6. Joos KM, Shen JH, Shetlar DJ, Casagrande VA. Optic nerve sheath fenestration with a novel wavelength produced by the free electron laser (FEL). Lasers Surg Med. 2000; 27(3):191–205. [PubMed: 11013381]

7. Joos KM, Mawn LA, Shen JH, Casagrande VA. Chronic and acute analysis of optic nerve sheath fenestration with the free electron laser in monkeys. Lasers Surg Med. 2003; 32(1):32–41. [PubMed: 12516068]

8. Joos KM, Mawn LA, Shen JH, Jansen ED, Robinson RD, Mackanos MA, Mavity-Hudson JA, Casagrande VA. Human optic nerve sheath fenestration with the free electron laser (FEL). Invest Ophthalmol Vis Sci. 2004; 45 E-Abstract 45.

9. Joos KM, Mawn LA, Shen JH, Jansen ED, Casagrande VA. Acute optic nerve sheath fenestration in humans using the free electron laser (FEL): a case report. Proc SPIE-Int Soc Opt Eng. 2002; 4611:81–85.

10. Shah RJ, Shen JH, Joos KM. Endoscopic free electron laser technique development for minimally invasive optic nerve sheath fenestration. Lasers Surg Med. 2007; 39:589–596. [PubMed: 17868109]

11. Edwards G, Hutson MS, Hauger S, Kozub J, Shen J, Shieh C, Topadze K, Joos KA. Comparison of OPA and Mark-III FEL for Tissue Ablation at 6.45 Microns. Proceedings of SPIE. 2002; 4633:194–200.

12. Mackanos MA, Simanovskii D, Joos KM, Schwettman HA, Jansen ED. Mid Infrared Optical Parametric Oscillator (OPO) as a Viable Alternative to Tissue Ablation With the Free Electron Laser (FEL). Lasers Surg Med. 2007; 39:230–236. [PubMed: 17304561]

13. Edwards GS, Pearlstein RD, Copeland ML, Hutson MS, Latone A, Spiro A, Pasmanik G. 6450-nm Wavelength Tissue Ablation Using a Nanosecond Laser Based on Difference Frequency Mixing and Stimulated Raman Scattering. Opt Lett. 2007; 32:1426–1428. [PubMed: 17546143]

14. Kozub J, Ivanov B, Jayasinghe A, Prasad R, Shen J, Klosner M, Heller D, Mendenhall M, Piston DW, Joos KA, Hutson MS. Raman-shifted alexandrite laser for soft tissue ablation in the 6- to 7-μm wavelength range. Biomed Opt Express. 2011; 2(5):1275–1281. [PubMed: 21559139]

15. Mackanos MA, Ivanov B, Soldatov AN, Kostadinov I, Mendenhall MH, Piston DW, Haglund RF, Jansen ED. Ablation of soft tissue at 6.45 μm using a strontium vapor laser. Proc SPIE-Int Soc Opt Eng. 2003; 5319:201–208.

16. Wada S, Tashiro H, Urata Y, Thi Thi L, Kasai A, Toyoda K. Two-stage Raman convertor covering the whole infrared spectrum with tunable solid-state lasers. Appl Phys B. 1993; 57(6):435–439.

17. Kozub JA, Shen J-H, Joos KM, Prasad R, Hutson MS. Efficacy and predictability of soft tissue ablation using a prototype Raman-shifted alexandrite laser. Journal of Biomedical Optics. 2015; 20(10):105004. [PubMed: 26456553]

18. Bliss CI. The Method of Probits. Science. 1934; 79(2037):38–39. [PubMed: 17813446]

19. Shen JH, Harrington JA, Edwards GS, Joos KM. Hollow-glass waveguide delivery of an infrared free-electron laser for microsurgical applications. Appl Opt. 2001; 40(4):583–587. [PubMed: 18357034]

20. Hutson MS, Ivanov B, Jayasinghe A, Adunas G, Xiao Y, Guo M, Kozub J. Interplay of wavelength, fluence and spot-size in free-electron laser ablation of cornea. Optics Express. 2009; 17:9840–9850. [PubMed: 19506634]

21. Burnham, KP.; Anderson, DR. Model Selection and Multimodel Inference: A Practical Information-Theoretic Approach. Springer-Verlag; New York: 2002.

22. Maralani PJ, Hassanlou M, Torres C, Chakraborty S, Kingstone M, Patel V, Zackon D, Bussiere M. Accuracy of brain imaging in the diagnosis of idiopathic intracranial hypertension. Clin Radiol. 2012; 67(7):656–663. [PubMed: 22309765]

23. Joos KM, Shen JH. Miniature real-time intraoperative forward-imaging optical coherence tomography probe. Biomed Opt Express. 2013; 4(8):1342–1350. [PubMed: 24009997]

24. Li ZY, Shen JH, Kozub JA, Prasad R, Lu PC, Joos KM. Miniature forward-imaging B-scan optical coherence tomography probe to guide real-time laser ablation. Lasers Surg Med. 2014; 46(3):193–202. [PubMed: 24648326]

25. Leung BY, Webster PJ, Fraser JM, Yang VX. Real-time guidance of thermal and ultrashort pulsed laser ablation in hard tissue using inline coherent imaging. Lasers Surg Med. 2012; 44(3):249–256. [PubMed: 22241665]
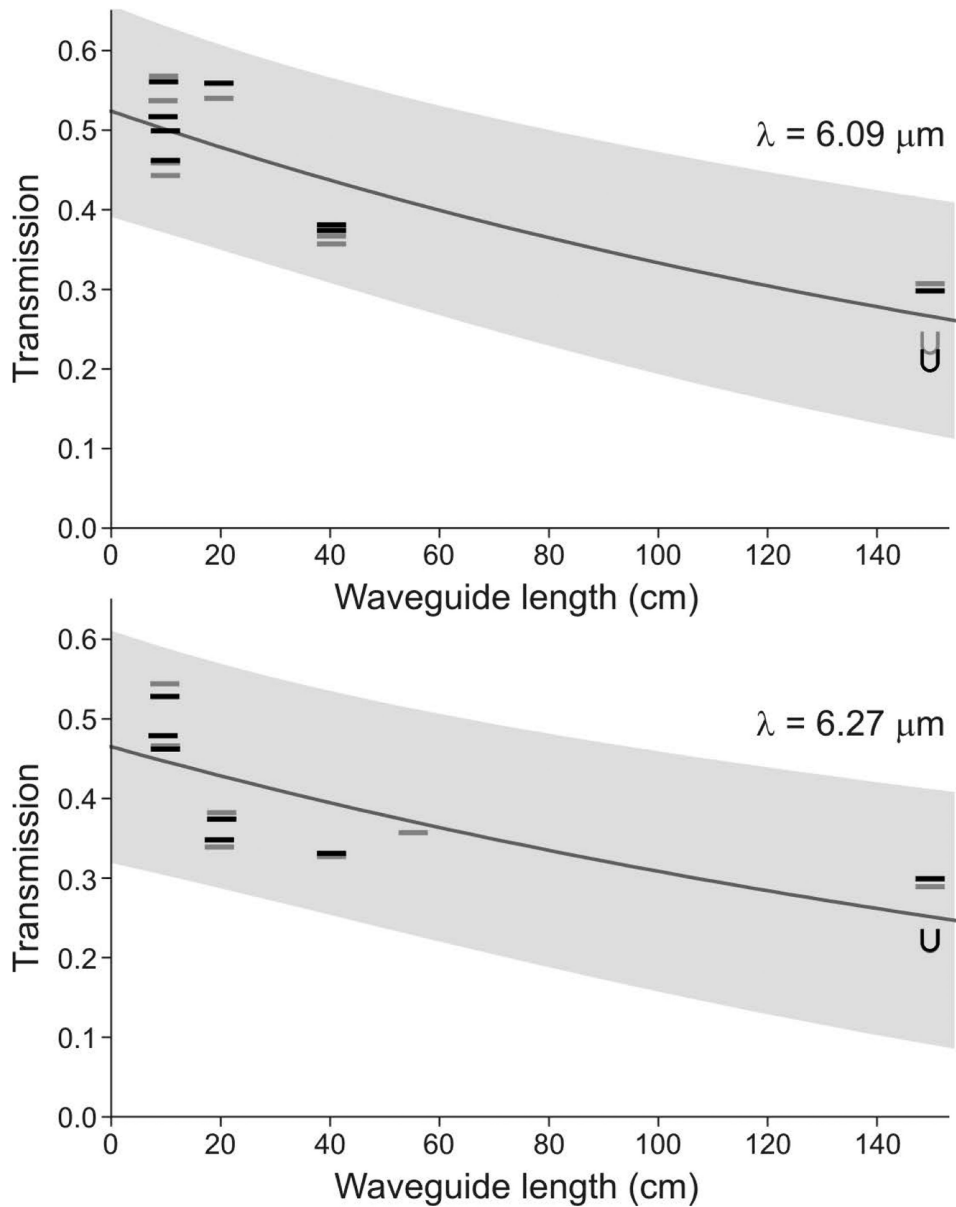
Figure 1.
Transmission through short sections of a 250-μm I.D. hollow-glass waveguide as a function of waveguide length. Each wavelength used measurements for two incident pulse energy ranges: 2.0-2.5 mJ (*black*) and 1.0-1.5 mJ (*gray*). The solid line is an exponential fit with shaded areas indicating 95% single prediction confidence intervals. The U symbols designate transmission through a 150-cm long waveguide with a sharp 90° bend having a radius of curvature of just 4.6 cm. These data points were not included for the exponential fits.
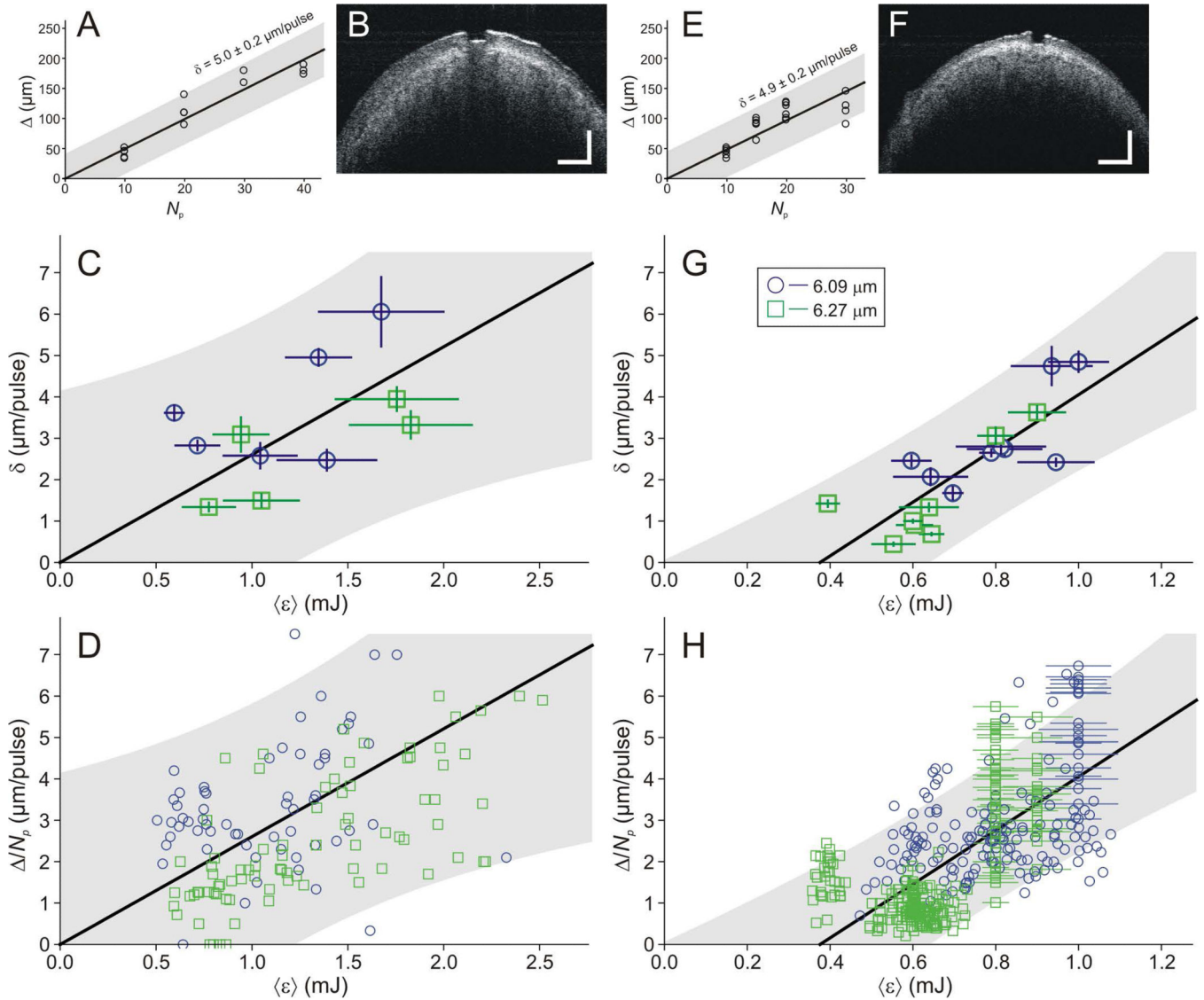
Figure 2.
Etch rate as a function of wavelength, average pulse energy and beam delivery method: **(A-D)** free-space delivery, focused to a spot diameter of 300 μm; **(E-H)** delivery through a 1.5-m long hollow-glass waveguide with a near-tip spot diameter of 200 μm. **(A, E)** Example plots of total crater depth, , versus number of pulses delivered. Both examples achieved etch rates close to 5 μm/pulse using a laser wavelength of 6.09 μm. Average pulse energies were 1.3 and 1.0 mJ, respectively. *Open symbols* denote depths of individual craters. *Solid lines* (and *shaded regions*) are best-fit linear regressions (and 95% confidence bands) for (N) with fixed zero offset. **(B, F)** Example OCT images used to measure crater depths in unfixed tissue. Scale bars are 500 μm in each direction. **(C, G)** Compilation of fitted etch rates, δ_{fit}, as measured by slopes of (N). Each *open symbol* represents the fitted slope to (N) for all craters ablated in a single sample using the same nominal laser parameters; *x*- and *y*-error bars respectively denote ± one standard error of the mean pulse energy and ± one standard error for δ_{fit}. *Thick solid lines* (and *shaded regions*) are best-fit linear regressions

(and 95% confidence bands) for combined data from both wavelengths. **(D, H)** Compilation of etch rates for individual craters, $\delta = /N$, versus average pulse energy, $<\varepsilon>$. Each *open symbol* represents a single crater. When individual pulse energies were not measured during a particular exposure, the average pulse energy was taken from pre-ablation measurements and error bars were added for these points to extend ± one standard error of the mean. *Thick solid lines* and *shaded regions* are an overlay of the regression from (C, G). Wavelength legend in (G) applies to (C, D, G, H).
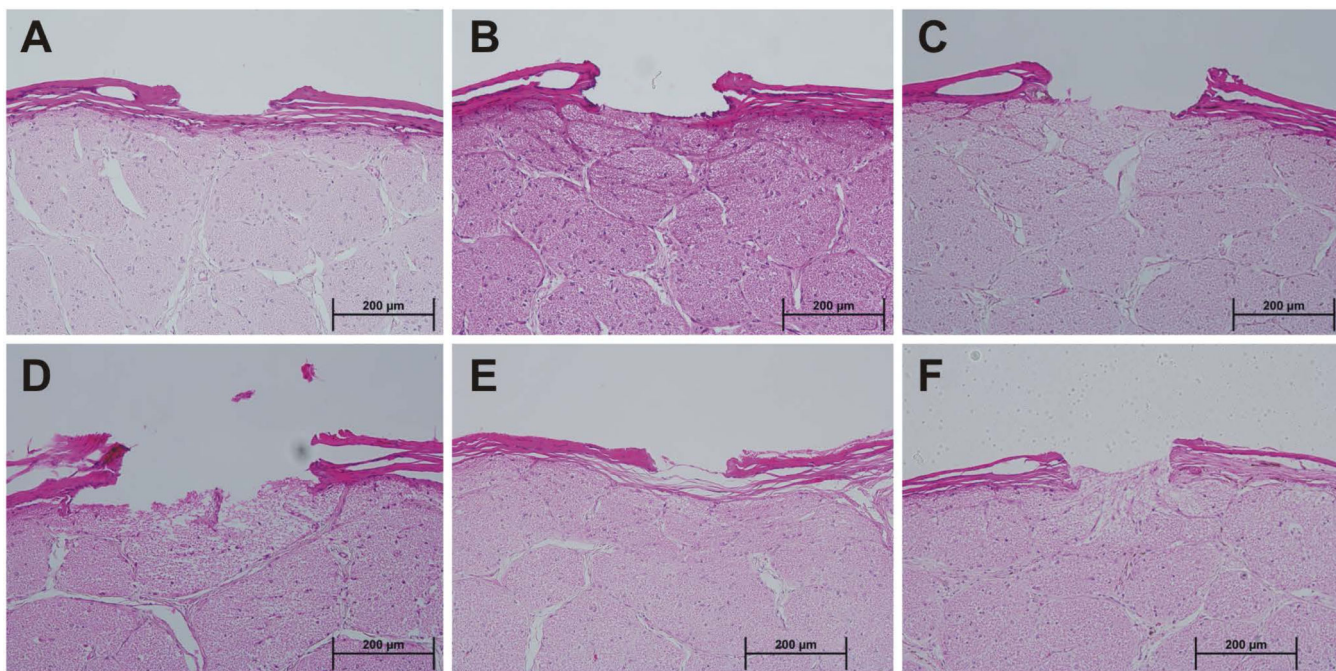
Figure 3.
Histological analysis of collateral damage to nerve sheath and underlying optic nerve after single point ablation. The RSA laser was tuned to λ = 6.09 μm and light was delivered through an endoscope with a 250-μm I.D. hollow glass waveguide: (**A**) 30 pulses at 0.8 mJ/pulse yielding ideal sheath perforation with no damage to underlying nerve; (**B**) same exposure conditions, but with pressure-induced damage to the nerve; (**C**) same conditions, but resulting in over-exposure where the ablation crater extended into the nerve; (**D**) 40 pulses at 0.8 mJ/pulse, which uniformly ablated through the sheath and into the underlying nerve; (**E**) 15 pulses at 1.0 mJ/pulse with ideal perforation, but some evidence of underlying neural compression; and (**F**) 30 pulses at 1.0 mJ/pulse that perforated the sheath and exposed the underlying nerve, which swelled up through the incision. Scale bar in each image is 200 μm.
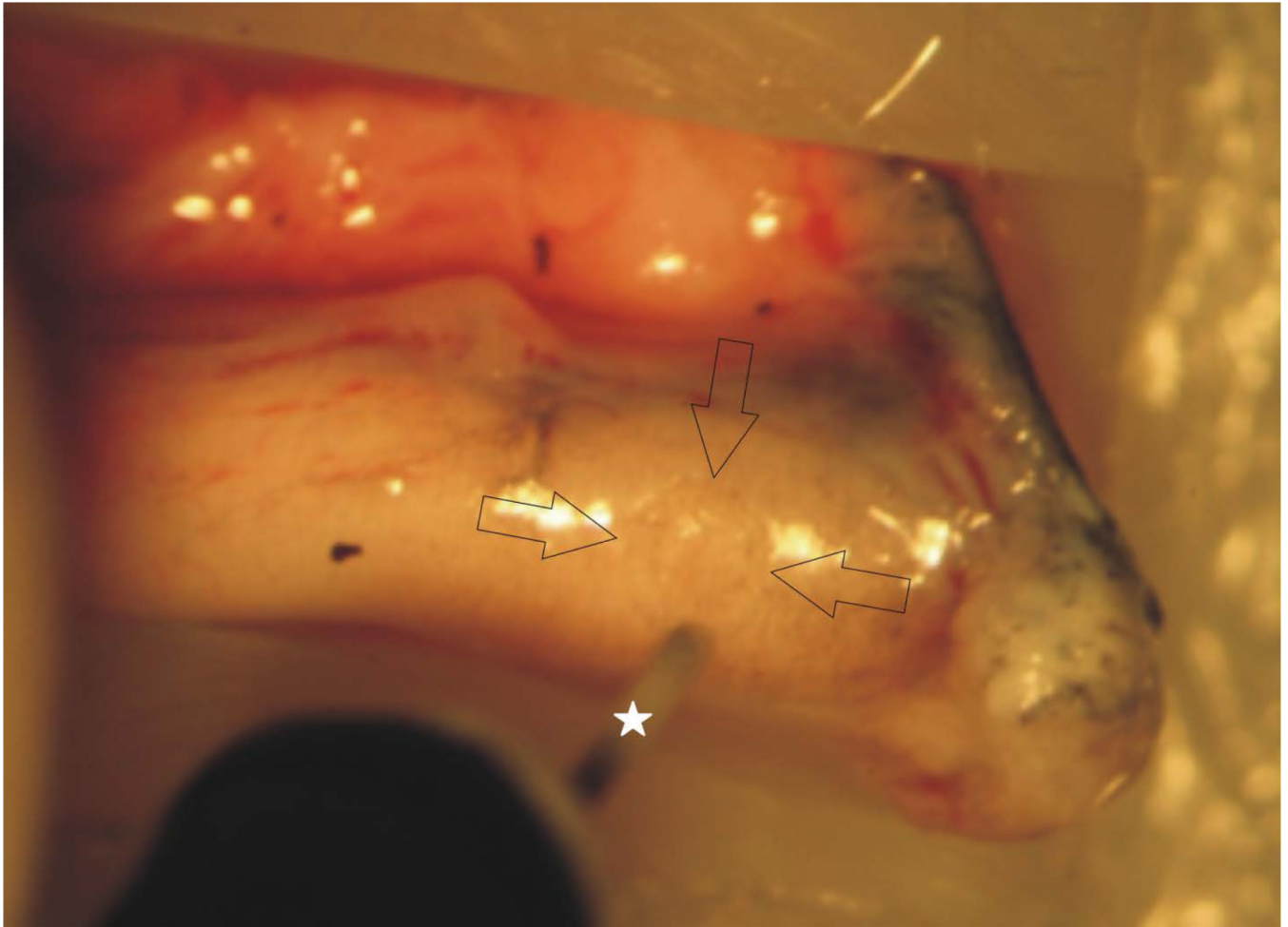
Figure 4.
Brightfield image of an *ex vivo* optic nerve immediately after its nerve sheath was fenestrated using the RSA laser tuned to a wavelength of 6.09 μm and delivered through an endoscope with a 250-μm I.D. hollow glass waveguide. The white star marks the waveguide tip extending from the endoscope. The waveguide tip and three arrows point to the margins of the circular incision (~ 1.5 to 2 mm in diameter).
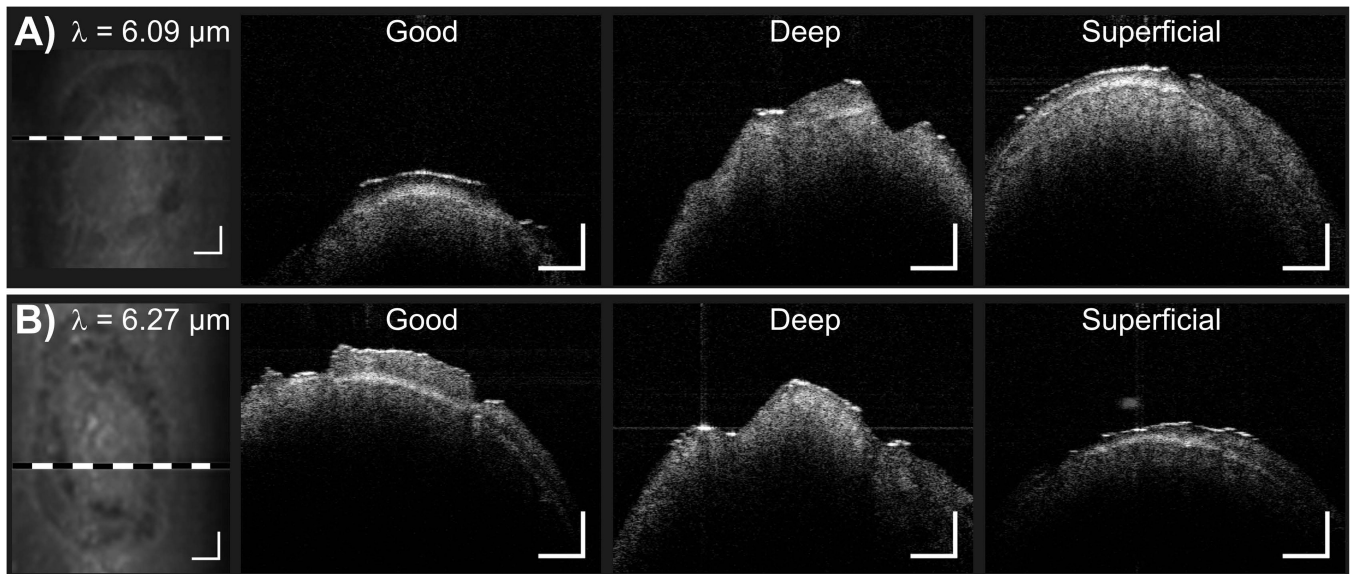
Figure 5.
Example OCT images taken immediately after laser exposure to evaluate the quality of *ex vivo* optic nerve sheath fenestration. Each row shows a surface profile of a good circular incision followed by three OCT cross-sections of attempted fenestrations that were respectively evaluated as good, too deep or too superficial. Laser wavelength was 6.09 μm in **(A)** and 6.27 μm in **(B)**. Dashed white lines on surface profiles mark the plane shown for "Good" cross-sections. Scale bars are 500 μm in each direction.
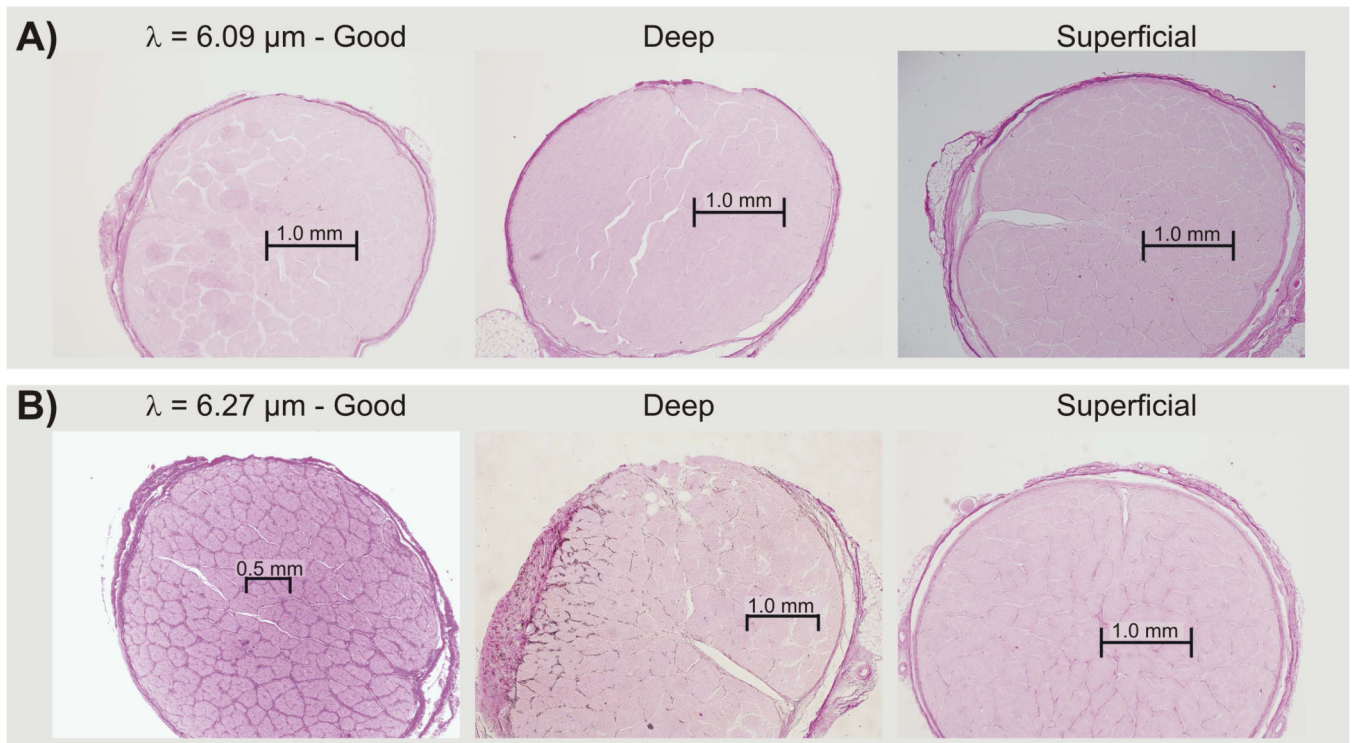
Figure 6.
Example histological images (H&E staining) of optic nerve cross-sections after *ex vivo* sheath fenestration. Each row shows three OCT cross-sections of attempted fenestrations that were respectively evaluated as good, too deep or too superficial. Laser wavelength was 6.09 μm in (**A**) and 6.27 μm in (**B**).

Table 1

Waveguide Coupling and Transmission

Wavelength (μm)	Coupling efficiency	1/e decay length (cm)
6.09	0.52 ± .02	220 ± 50
6.27	0.46 ± .02	240 ± 70

Table 2

Ablation Thresholds

Delivery Method	Spot Diameter (μm)	Wavelength (μm)	Threshold Energy (mJ)	Threshold Fluence (J/cm²)
Free-space	300 ± 20	6.09	0.13 ± 0.02	0.18 ± 0.04
		6.27	0.24 ± 0.03	0.34 ± 0.06
		6.43	> 0.5	> 0.7
Waveguide	200 ± 20	6.09	0.26 ± 0.03 [*]	0.8 ± 0.2 [*]
		6.27	0.48 ± 0.03 [*]	1.5 ± 0.3 [*]
		6.43	~0.56 [**]	~1.6 [**]

[*] Measured through a 1.5-m long waveguide.

[**] Measured through just an 8-cm length of waveguide.

Table 3

Ablation Rates

Delivery Method	Spot Diameter (μm)	Wavelength (μm)	Mean Energy (mJ)	Mean Fluence (J/cm^2)	Ablation Rate (μm/pulse)
Free-space	300 ± 20	6.09	0.7	1.0	2-3
			1.3	1.8	3-6
			1.5	2.1	6-10[*]
		6.27	0.8	1.1	1-3
			1.1	1.6	2-5
			1.8	2.5	5-8[*]
		6.45	1.0	1.4	not measurable
Waveguide	200 ± 20	6.09	0.6	1.9	1-3
			0.8	2.5	2-4
			1.0	3.2	4-6[*]
		6.27	0.6	1.9	0.5-1
			0.85	2.7	2-5[*]
		6.43	1.0	3.2	not measureable

[*] These conditions often, but not always, resulted in perforation of nerve sheaths within 1-3 s. When the nerve sheath was perforated, a minimum etch rate was estimated based on the sheath thickness.

Table 4

Evaluation of fenestration quality.

Wavelength (μm)	# nerves exposed	# good (%)	# deep (%)	# superficial (%)
6.09 μm	48	16 (33%)	23 (48%)	9 (19%)
6.27 μm	11	4 (36%)	2 (18%)	5 (45%)